nature communications

Article

https://doi.org/10.1038/s41467-025-57287-7

GORK K^+ channel structure and gating vital to informing stomatal engineering

Received: 6 September 2024

Accepted: 18 February 2025

Published online: 25 February 2025

Check for updates

Xue Zhang[1,2,4], William Carroll[3,4], Thu Binh-Anh Nguyen[3,4], Thanh-Hao Nguyen[3], Zhao Yang[1,2], Miaolian Ma[1,2], Xiaowei Huang[1], Adrian Hills[3], Hui Guo[1,2], Rucha Karnik[3], Michael R. Blatt[3,5] ✉ & Peng Zhang[1,2,5] ✉

The *Arabidopsis* GORK channel is a major pathway for guard cell K^+ efflux that facilitates stomatal closure. GORK is an outwardly-rectifying member of the cyclic-nucleotide binding-homology domain (CNBHD) family of K^+ channels with close homologues in all other angiosperms known to date. Its bioengineering has demonstrated the potential for enhanced carbon assimilation and water use efficiency. Here we identify critical domains through structural and functional analysis, highlighting conformations that reflect long-lived closed and pre-open states of GORK. These conformations are marked by interactions at the cytosolic face of the membrane between so-called voltage-sensor, C-linker and CNBHD domains, the latter relocating across 10 Å below the voltage sensor. The interactions center around two coupling sites that functional analysis establish are critical for channel gating. The channel is also subject to putative, ligand-like interactions within the CNBHD, which leads to its gating independence of cyclic nucleotides such as cAMP or cGMP. These findings implicate a multi-step mechanism of semi-independent conformational transitions that underlie channel activity and offer promising new sites for optimizing GORK to engineer stomata.

Stomata are pores that mediate gaseous exchange across the impermeable surface of plant leaves. They open in the light to allow CO_2 entry for photosynthesis and close to prevent leaf drying. Guard cells surrounding each stoma regulate the aperture in response to environmental and internal signals through the uptake and release of osmotically-active solutes and water[1–3]. Ionic potassium (K^+) is the predominant inorganic solute transported by guard cells and is taken up by voltage-dependent K^+ channels and H^+-coupled symport[4,5] and is released through a second set of K^+ channels.

The GORK K^+ channel was first identified with the *gork* null mutant that slows stomatal closing[6–8] and is a major pathway mediating K^+ efflux for stomatal closure. GORK is a member of the cyclic-nucleotide binding (homology) domain (CNBD/CNBHD) channel subfamily, and exhibits unique regulatory characteristics that appear to be conserved among these channels in angiosperm plants[9–11]. Like other outward-rectifying K^+ channels of plants[12,13], GORK is activated with membrane depolarisation to voltages positive of the K^+ equilibrium voltage[7,14]. External K^+ acts as an inhibitor of the gate so that the voltage dependence for activation is shifted in the positive direction with increasing K^+ outside[11]. The action was interpreted previously as a 'failsafe' to prevent K^+ uptake when K^+ rises around the guard cells[9,13]. These characteristics of K^+ dependence are intrinsic to the GORK

[1]National Key Laboratory of Plant Molecular Genetics, CAS Centre for Excellence in Molecular Plant Sciences, Institute of Plant Physiology and Ecology, Shanghai, China. [2]Key Laboratory of Plant Carbon Capture, Chinese Academy of Sciences, Shanghai 200032, China. [3]Laboratory of Plant Physiology and Biophysics and School of Molecular Biosciences, Bower Building, University of Glasgow, Glasgow G12 8QQ, UK. [4]These authors contributed equally: Xue Zhang, William Carroll, Thu Binh-Anh Nguyen. [5]These authors jointly supervised this work: Michael R. Blatt, Peng Zhang.
✉e-mail: michael.blatt@glasgow.ac.uk; pengzhang01@cemps.ac.cn

protein and are retained when the channel is expressed in *Xenopus laevis* oocytes[7,14,15].

Previous work showed that relaxing the K^+ dependence of GORK gating accelerates steady-state K^+ flux, thereby enhancing stomatal kinetics and carbon assimilation in fluctuating environments typically experienced by plants in the field[15]. These findings mark the GORK channel as a promising target in extending bioengineering, both to enhance carbon capture and to improve water use efficiency[16]. As a key step in this direction, and to understand the unusual mechanics of GORK gating, we undertook a structural analysis of the channel in conjunction with functional studies to resolve sites within GORK that are important for its unique gating. Our results highlight two coupling sites and their interactions that have major impacts on GORK gating. These sites and the associated conformations indicate an unprecedented, latching mechanism of semi-independent elements that operate in concert to gate the channel.

Results

GORK architecture

For single-particle cryo-EM structural studies, the *Arabidopsis* full-length GORK was expressed as a fusion protein with Green Fluorescent Protein (GFP) in sf9 insect cells. Initially, the wild-type protein (GORK or $GORK^{wt}$) was purified in a 150 mM KCl and 0.02% glyco-diosgenin (GDN) environment. The cryo-EM analysis revealed the density map of a homotetramer at 3.0 Å resolution. Focused refinement was employed to improve the resolution of the cytosolic region and facilitate atomic model construction of 688 residues of the core GORK structure (Fig. 1a; Supplementary Figs. 1, and 2). This final structure

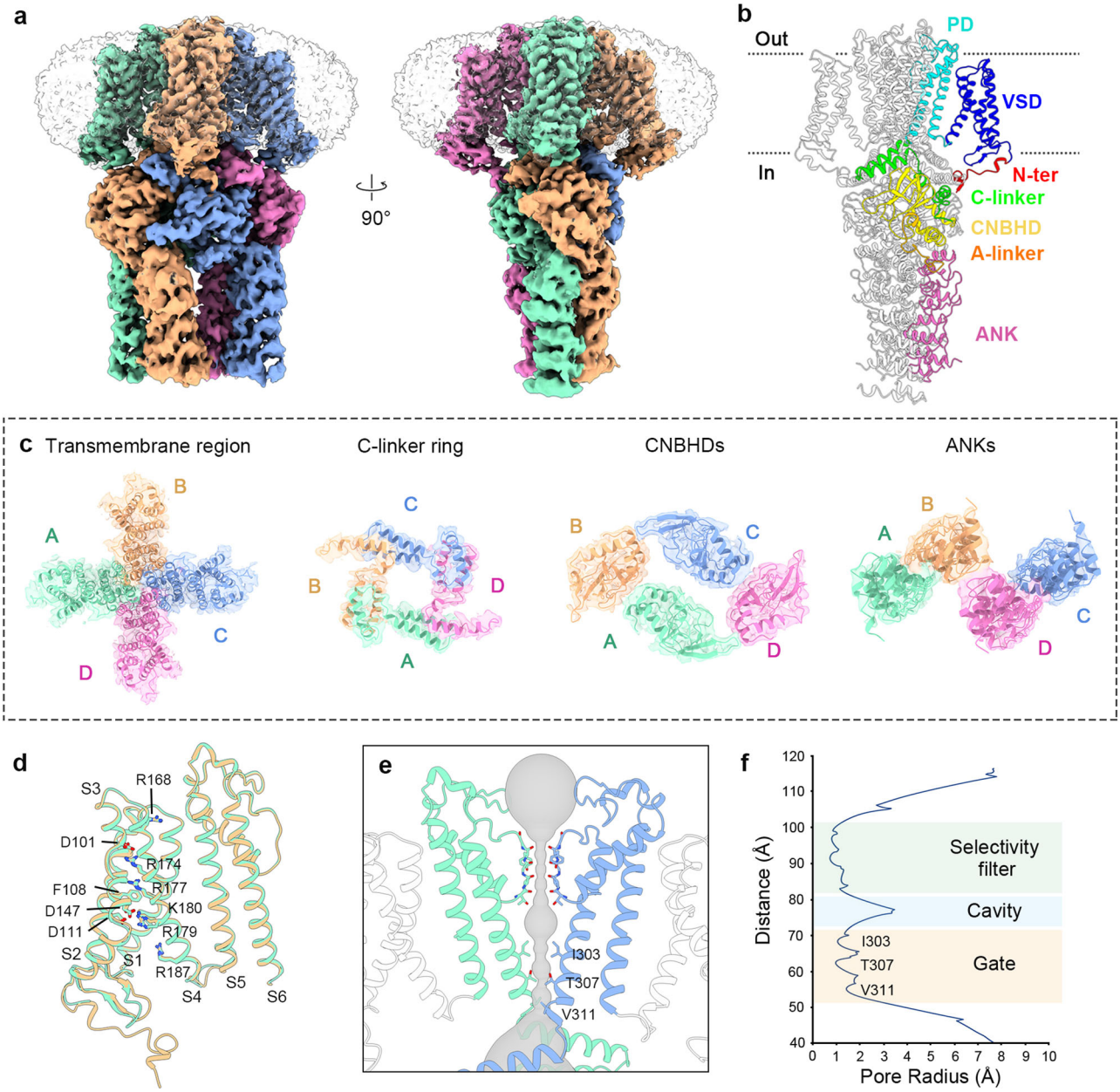

Fig. 1 | Architecture of GORK. a Cryo-EM density for 3D reconstruction of GORK, with four subunits coloured in green, yellow, blue, and pink, and micelle densities coloured in light grey. **b** Side view of cartoon representation of GORK, with one subunit highlighted and coloured by domains. **c** Domain layers viewed sectionally from inside with subunits labelled (A-D). **d** Side view of the VSD and PD of neighbouring subunits. Stick side chains are shown for the gating-charge residues, counter-charge residues and hydrophobic constriction site. **e** Ion conduction pore of GORK with front and rear subunits removed for clarity. Ion permeation pathway is shown in grey. Gating residues and filter residues are shown as sticks. **f** Pore radius calculated by MOLE. The constricting residues are labelled.

comprised part of the cytosolic N-terminus, the transmembrane domains of the channel, and most of the cytosolic region of the protein including the CNBHD and the ANK domains (Fig. 1b). Missing only were the first 32 residues of the N-terminus and the final C-terminal region of 100 residues.

Without constraints, the GORK tetramer adopted a fourfold symmetry within the transmembrane region that collapsed to two-fold symmetry within the C-terminal cytosolic region (Fig. 1c). Within the transmembrane region, the four subunits of GORK aligned to a non-domain-swapped architecture of six α-helices (S1–S6) with the voltage-sensor domain (VSD, S1–S4) positioned against the pore domain (PD, S5–S6) of the same subunit (Fig. 1d). Evident below the VSD on the cytosolic membrane face, we resolved an elbow-on-shoulder ring of C-linkers. Each C-linker comprised of a hairpin of two helices (A′ and B′) and two shorter helical sequences (C′ and D′) that are a feature of CNBD channels characterised to date[17–24] (Supplementary Figs. 3 and 4; see also Fig. 1b, c) and bridge the PD and CNBHD sequences. The C-linkers appeared to form a transition zone with alternating configurations within the same reconstruction: adjacent subunits—hereafter designated A through D, with pairings A/B and C/D—formed a stable interface through the CNBHDs that extended into two separate strands of two-fold symmetry in the ANK domains (Fig. 1c). These characteristics ally GORK with the plant K^+ channels AKT1[24] and SKOR[23] and distinguish GORK from other CNBD channels (Supplementary Fig. 3).

A more detailed analysis showed, within the VSDs, a regularly-spaced sequence of six positively-charged residues in the S4 helix contribute to the gating charge movements, with counter-charges residing on the S2 and S3 helices and residue F108 from the S2 helix forming a hydrophobic constriction over which the S4 residues pivot (Fig. 1d). In general, the VSDs of K^+ channels assume an 'up' conformation on membrane depolarisation that favours movement of these charged residues away from the cytosolic face of the membrane and re-aligns the counter-charges across a constriction formed by residue F108. We observed residues R168, R174, and R177 to locate above, and R179, K180 and R187 to locate below F108. This arrangement is consistent with the 'up' position of the VSD as expected of the channel when isolated in the absence of an electrical field.

Like other K^+ channels, within the PD the GORK channel assembly forms a 'bracelet' of backbone carbonyls from the signature TVGYG motif. The carbonyls coordinate K^+ ions as they pass through this filter[25,26] and showed a density associated with a string of K^+ ions in the filter (Fig. 1e). Below the filter, the internal gate of the pore is formed by the side chains of residues I303, T307 and V311 at the base of the S6 helix. We found that these residues formed a constriction of approximately 1 Å, indicating that the channel was closed (Fig. 1e-f). While the 'up' conformation of the VSD might imply an open state of the channel, we note that the K^+-dependence of GORK prevents channel opening in high K^+ [7,12,13,15]. In the closely related SKOR K^+ channel, increasing external K^+ concentrations introduce a long-lived closed state, even at depolarising voltages, that gives rise to K^+ inhibition[27]. GORK evidently adopts a closed state in 150 mM K^+, even with the VSD in the 'up' conformation. Thus, it is reasonable to conclude that the structure represents a similar, long-lived channel conformation, presumably inhibited by high potassium concentration.

Coupling sites

The four to twofold symmetry reduction of GORK is shaped by distinct configurations of the C-linker and, between the CNBHD and ANK domains, a region we have designated the ankyrin- or A-linker. Both linkers adopt a 'flat' conformation of helical structures in subunits A and C; the corresponding linkers in subunits B and D display a 'kinked' conformation with lower helical content that implies increased flexibility (Fig. 2a, b and Supplementary Fig. 4a). The two kinked subunits B and D associate with CNBHDs that are raised to abut closely with the C-linker and VSD, while subunits A and C position the CNBHDs 10 Å lower below the corresponding C-linker and VSD.

These variations in linker regions highlighted two putative coupling sites of likely importance for channel kinetics (Fig. 2a, b and Supplementary Fig. 4b). The first and most tightly packed coupling site (Coupling Site I, CSI) is located below the pore domain where the S4 and S5 helices overlay the C-linkers (Fig. 2c-d). Here residue R320 from the C-linker A′ helix abuts the S4–S5 loop of adjacent subunit, forming hydrogen bonds with the backbone of vicinal residues. Two K312 residues at the base of the S6 helix in subunits A and C interact with E317 and D321 of the C-linker A′ helices in subunits B and D (Fig. 2c, Supplementary Fig. 5a, c); the other two K312 residues of subunits B and D interact with D321 and Y196 of the C-linker helices of subunits A and C (Fig. 2d, Supplementary Fig. 5b, d). The net effect is to generate a tight necklace of salt-bridges and hydrogen-bonds between the subunit pairs and immediately below the pore gate. It is noteworthy that D321 and the linkages it forms are partially-conserved among other CNBD channels, including AKT1, KAT1, and HCN1[18,24,28] and fully conserved in SKOR[23].

Prior to resolving the GORK structure our functional analyses drew on homologies to AKT1 and SKOR. We generated GORK mutants, substituting each residue with Ala and with residues introducing opposing charges before expressing the mutated channels in oocytes for functional assessment. Unlike some plant CNBD K^+ channels[11,29,30], functional activity of GORK in oocytes does not require co-expression with protein kinases to activate the current[14,15]. Voltage clamp analysis in *Xenopus* oocytes showed that, with some notable exceptions, many substitutions around CSI failed to yield functional channels (Supplementary Fig. 5e). The findings drew our attention to this coupling site. In addition to the $GORK^{K312R}$ mutant, the mutants $GORK^{E317A}$ and $GORK^{D321A}$ each yielded ensemble, or whole-cell, currents roughly 2-fold greater in amplitude than the wild-type GORK; the currents also activated rapidly on depolarisation and deactivated slowly on repolarization when compared with $GORK^{wt}$ (Fig. 2e). Substitutions to give $GORK^{E317Q}$ and $GORK^{D321N}$, eliminating the negative charged side groups, further enhanced the ensemble conductance (Fig. 2f), accelerated activation on membrane depolarisation and slowed deactivation on repolarization. Substitutions introducing positively-charged side chains with $GORK^{E317K}$ and $GORK^{D321R}$ failed to yield currents (Supplementary Fig. 5e).

We analysed the current from each construct to extract the gating characteristics of the midpoint voltage, $V_{1/2}$, and apparent voltage sensitivity or gating charge, δ, as well as the maximum ensemble (whole-cell) conductance, G_{max} (see "Methods"). Additionally, we calculated the relative conductance (G/G_{max}) from tail current amplitudes recorded at −140 or −160 mV (see "Methods"). In general, fittings gave values of δ of 1.6–1.8 in every case, consistent with the channel in vivo[14,15]. However, fitting the steady-state currents of $GORK^{E317A}$ and $GORK^{D321A}$ to a Boltzmann function (Eq. [1], see "Methods") showed highly significant negative shifts in the midpoint voltage for gating, $V_{1/2}$, relative to $GORK^{wt}$ to values of −37 ± 2 and −34 ± 4 mV, shifts that were evident also in G_{rel} determined from tail currents (Fig. 2f). The features of $GORK^{E317A}$ and $GORK^{D321A}$ were strongly enhanced in the double mutant $GORK^{E317AD321A}$ (Fig. 2e, f). Current in the double mutant deactivated with halftimes near 10 s and yielded a shift in $V_{1/2}$ of −43 ± 3 mV, indicating almost a 2 kcal mol^{-1} reduction in the energy barrier for activating the channel[31]. These findings again indicated a critical role for the coupling between the C-linker ring and the base of the pore.

We used these functional studies to guide cryo-EM analysis of the full-length $GORK^{E317AD321A}$ protein. The mutant yielded a stable transmembrane region but showed a loss of density resolution, notably below the CNBHD, suggesting much greater conformational dynamics within the cytosolic C-terminal region. After focused 3D classification to mask the PD and the C-linker, we obtained a relatively complete

https://doi.org/10.1038/s41467-025-57287-7

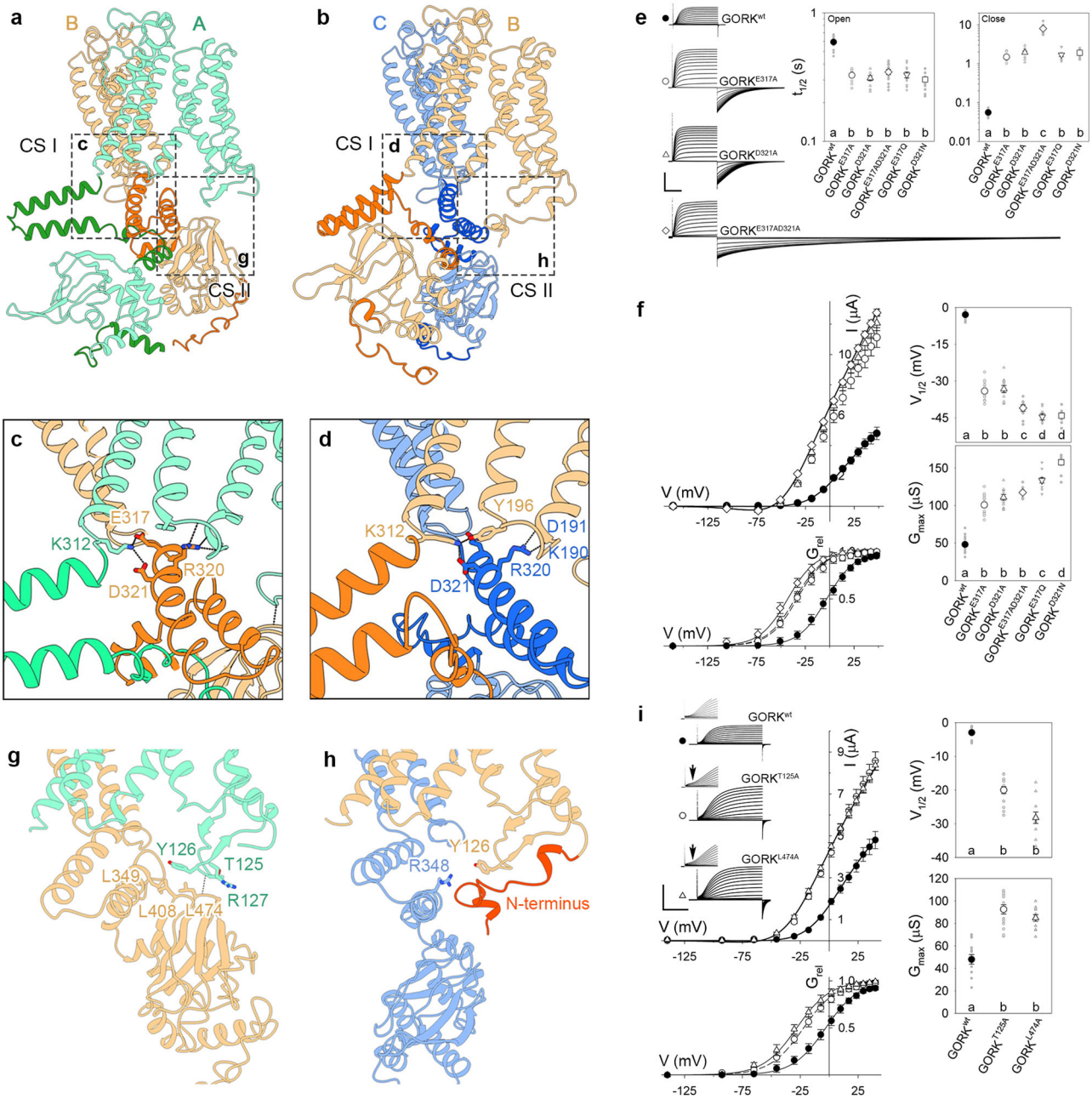

Fig. 2 | Coupling sites and GORK channel kinetics. a, **b** Two major coupling sites formed by adjacent pairs of neighbouring subunits, with the other subunit pairs removed in each for clarity. The C-linker and A-linker domains are indicated by darker colours. **c**, **d** Close-up view of Coupling Site I (CSI) cross-referenced to (**a**, **b**). Key residues are shown as sticks. **e** Mutants of CSI residues E317 and D321 accelerate activation and slow deactivation of GORK. Representative voltage clamp traces (*left*) for GORK^{wt}, GORK^{E317A}, GORK^{D321A} and GORK^{E317AD321A}. Scale: vertical, 5 μA; horizontal, 2 s. Halftime ($t_{1/2}$) analysis for activation at +40 mV (*centre*) and deactivation at −140 mV (*right*) cross-referenced to traces by symbol. Note the logarithmic scales. Data from $n > 12$ independent experiments for each construct (*small grey symbols*) are shown with means ± SEM (*large symbols*). Lettering indicates significant differences at $P < 0.002$. **f** Steady-state current–voltage curves (*left, above*) and relative conductance–voltage curves (*left, below*) are means ± SEM ($n > 12$) from the data in (**e**). Gating parameters (*right*) of midpoint voltage ($V_{1/2}$) and maximum ensemble conductance (G_{max}) are from fittings to Eq. [1]. Relative conductance plots are overlaid with means ± SEM of tail currents after scaling to G_{max} taken from fittings to Eq. [1]. Data for each construct (*small grey symbols*) are shown with means ± SEM (*large symbols*) cross-referenced by symbol. Lettering indicates significant differences at $P < 0.002$. Fittings for GORK^{wt} and GORK^{E317AD321A} shown (*left*) for visual guidance. **g**, **h** Close-up view of Coupling Site II (CSII) cross-referenced to (**a**, **b**). Key residues are shown as sticks. N-terminus is coloured in orange in (**h**). **i** Voltage clamp analysis of GORK^{wt} and the CSII mutants GORK^{T125A} and GORK^{L474A}. Current-voltage (*centre, above*) and relative conductance-voltage curves (*centre, below*) are means ± SEM of $n > 12$ for each construct. Gating parameters (*right*) of midpoint voltage ($V_{1/2}$) and maximum ensemble conductance (G_{max}) are from fittings to Eq. [1]. Relative conductance plots are overlaid with means ± SEM of tail currents after scaling to G_{max} taken from fittings to Eq. [1]. Representative voltage clamp traces (*insets, left*) are cross-referenced by symbol; expanded scales are of the first 0.5 s of each clamp step with arrows marking the shoulders in activation. Scale: vertical, 4 μA; horizontal, 1 s. Analysis (*right*) for each independent experiment (*small grey symbols*) and means ± SEM (*large symbols*) shows negative shifts in $V_{1/2}$ and increase in G_{max} for GORK^{T125A} and GORK^{L474A} relative to GORK^{wt}. Lettering indicates significant differences at $P < 0.002$. Fittings for GORK^{wt} and GORK^{L474A} shown (*left*) for visual guidance. Immunoblots are included in Supplementary Fig. 10. Source data are provided as a Source Data file.

reconstruction (Supplementary Fig. 6). The resolved structure of GORK^{E317AD321A} showed a tilt of the S4–S5 loop and partial rotation of the C-linkers relative to GORK^{wt} (Supplementary Fig. 6f, g and Supplementary Movie 1). Given the substantial impact on gating evident for the GORK^{E317AD321A} mutant, these observations point to the CSI interactions and their relaxation as the likely explanation for the reduced energy barrier for gating.

Comparison of GORK^{wt} and GORK^{E317AD312A} also highlighted a second, putative coupling site (CSII) located below the VSD. This site arises between subunit pairs A/B and C/D with a proximal association between the base of the VSD S2–S3 loop, the C-linker and CNBHD (Fig. 2g, h). Here, the kinked C-linker and raised CNBHD abut the VSD of neighbouring subunit, with T125, Y126, R127 of the S2–S3 loop positioned against a hydrophobic patch formed by L349 of the C-linker and L408 and L474 of the CNBHD (Fig. 2g). We postulated that these interactions might impact on the raised CNBHD. To test this idea, we generated the substitutions GORK^{L474A} and GORK^{T125A}. Both mutants gave enhanced current amplitudes and displaced $V_{1/2}$ to −28 ± 4 mV and −19 ± 1 mV, respectively, both in Boltzmann fittings and tail current analyses (Fig. 2i). Evident in recordings from both mutants, too, was a shoulder in the kinetics for current activation (Fig. 2i, inset), consistent with the idea that interfering with the interactions of the VSD S2-S3 loop and CNBHD exposed an intermediate in the transition from the closed to open states.

We also suspected a possible intercalation in the B/C and D/A subunit pairs of an N-terminal segment between the flat C-linker and VSD (Fig. 2h), as modelling the N-terminal residues 33–47 satisfied the EM density and chemical environment (Supplementary Fig. 2). We generated an N-terminal deletion mutant, omitting the first 50 residues to give GORK$^{\Delta 50}$. Expressed in oocytes, GORK$^{\Delta 50}$ yielded roughly a 1.8-fold increase in current amplitude and $V_{1/2}$ shift of −30 ± 3 mV relative to GORK^{wt} (Supplementary Fig. 7a). Cryo-EM analysis of the GORK$^{\Delta 50}$ protein (Supplementary Fig. 7b–e) showed a dominant conformation that, with the lack of the N-terminus, positioned three of the four CNBHDs raised to abut the S2–S3 loops of the corresponding VSDs (Supplementary Fig. 7f and Supplementary Movie 2). These data are consistent with an N-terminal interaction in coupling the VSD and CNBHD, its deletion facilitating VSD-CNBHD coupling and thereby relaxing the channel gate to enhance activity[15].

A-linker and intrinsic-ligand-like interactions

Despite their widespread presence, there are hints that the CNBHDs found in the voltage-dependent channels of plants may have lost their capacity for cyclic-nucleotide binding[32]. Indeed, the β-roll structures known to coordinate cyclic nucleotides of binding CNBDs are not conserved among the plant K^+ channels[32]. Nonetheless, within the A-linker of subunits B and D we resolved a kink and short helix at the end of the CNBHD, positioning the side chain of residue R512 within the pseudo ligand-binding pocket (Fig. 3a). Neighbouring subunits A and C, by contrast, exhibited a flattened A-linker, forming a long helix with the first ANK repeat that left the corresponding pseudo-binding pockets exposed (Fig. 3b). Thus, two of the four subunits positioned R512 in the space that would typically be occupied by a cyclic nucleotide such as is bound in HCN1[17] (Fig. 3c). A similar mechanism is observed in the KCNH family members[21,33,34], where three residues of a β-strand motif function as an intrinsic ligand (Fig. 3d), mutation or deletion of which affects voltage-dependent gating[33,35,36]. We tested for a role of the CNBHDs in GORK with additions of membrane permeable 8-bromo-cAMP and 8-bromo-cGMP during recordings but observed no effect either on the voltage-dependence or ensemble conductance (Fig. 3e). However, charge-swapped and size-exclusion mutants GORK^{R512E}, GORK^{R512F} and GORK^{R512Q} reduced the ensemble conductance (Fig. 3f), suggesting that the residue R512 and its intercalation within the pseudo-binding pocket is important for channel conformations that support activity.

A cytosolic tetramer interface

Three further interacting regions were resolved within the cytosolic domain and, initially, were thought to be important for subunit assembly. The first region was evident within the ring of C-linkers (Fig. 4a and Supplementary Fig. 4b). Here, in the B/C and A/D subunit pairs, the residues D357 and D363 of the kinked C-linker subunits B or D appeared to form salt-bridges or hydrogen-bonds with residues R332 and K322 of the neighbouring subunits C or A. These interactions were seen to be replaced by coordination with T356-K333 and D363-T358 in the A/B and C/D subunit pairs. Analysis of GORK^{R332A} and GORK^{D357A} showed small, but significant positive shifts in gating evident in $V_{1/2}$ and 50–70% reductions in G_{max}; however, GORK^{T356A} and GORK^{K333A} had no significant effect on channel gating when compared to GORK^{wt} (Fig. 4b). A second region, arising between CNBHD surfaces in the subunit pairs A/B and C/D centred around Q397 and Y424 (Fig. 4c). Expressing GORK^{Q397A} gave a mean shift of $V_{1/2}$ to −19 ± 3 mV and 1.6-fold rise in G_{max}. The GORK^{Y424A} mutant gave only a modest shift in $V_{1/2}$, although it reduced G_{max} to roughly 40% of that for GORK^{wt} (Fig. 4b).

The third region arose with the tight pairing of neighbouring ANK domains of subunit A/B and C/D, and a weaker apposition of B and D at the last ANK repeat (Fig. 4d). This region has been proposed to contribute to tetramer assembly[37]. To assess the impact of this region on channel function, we generated the C-terminal deletions GORK$^{\Delta 527}$ and GORK$^{\Delta 702}$ thereby removing the K_{HA} + ANK and K_{HA} domains, respectively. Expressing these constructs showed small shifts in $V_{1/2}$ relative to GORK^{wt} that, like the effects on G_{max}, were not significant (Fig. 4e). However, that we recovered fully-functional channels with both deletions belies any critical role for the region in channel assembly and activity. Indeed, the substantial mobility, implicit in the loss of resolvable structures to the ANK and K_{HA} domains under conditions favouring channel activation (Supplementary Figs. 6 and 7), suggest that their conformations are dictated by the channel structure within, and immediately beneath the membrane surface, not the other way around.

A pre-open state

Extensive functional analysis of GORK[11,14,15] shows that the channel remains closed in high K^+, even at 0 mV such as experienced by the protein in isolation. This knowledge, and our structural observations (Fig. 1e, f), point to conformations of the closed channel. GORK gating is displaced to more negative voltages on mutation within the cytosolic N-terminus: Horaruang et al. [15] noted that mutations of the GORK N-terminus affecting channel clustering also displaced gating to render a channel that favoured the open state at 0 mV even in 50 mM K^+. Subsequently, we found that the GORK$^{\Delta 23}$ deletion mutant, lacking the N-terminal 23 residues, itself displaced $V_{1/2}$ for gating to −47 ± 1 mV (Fig. 5a), an effect greater than observed with GORK$^{\Delta 50}$.

To further bias the conditions for channel opening, we isolated the GORK$^{\Delta 23}$ protein in 10 mM K^+ for cryo-EM analysis (Supplementary Fig. 8). The analysis yielded a predominant structure lacking much detail beyond CNBHD in the cytosolic region but exhibiting four-fold symmetry with all four CNBHDs raised to abut against the corresponding C-linkers and VSDs (GORK$^{\Delta 23}$-sym) (Fig. 5b). Also classified were structures exhibiting nearly full-length and asymmetrical density maps (GORK$^{\Delta 23}$) and, among these, structures with three of the four CNBHDs in a raised configuration similar to the structures resolved with GORK$^{\Delta 50}$. Notable in GORK$^{\Delta 23}$-sym structure, we observed all four C-linkers in a kinked conformation placing each of the four K312 residues around the ring in opposition to the D321 residue from the same subunit (Fig. 5c and Supplementary Fig. 9a, b). Also evident in this structure, the four VSDs appeared to form hydrophobic interactions with CNBHDs, and were displaced by roughly 2 Å within the plane of the membrane and away from the pore-lining helices, compared with GORK^{wt}, leading to a 0.5–0.7 Å dilation of the channel gate at residues

https://doi.org/10.1038/s41467-025-57287-7

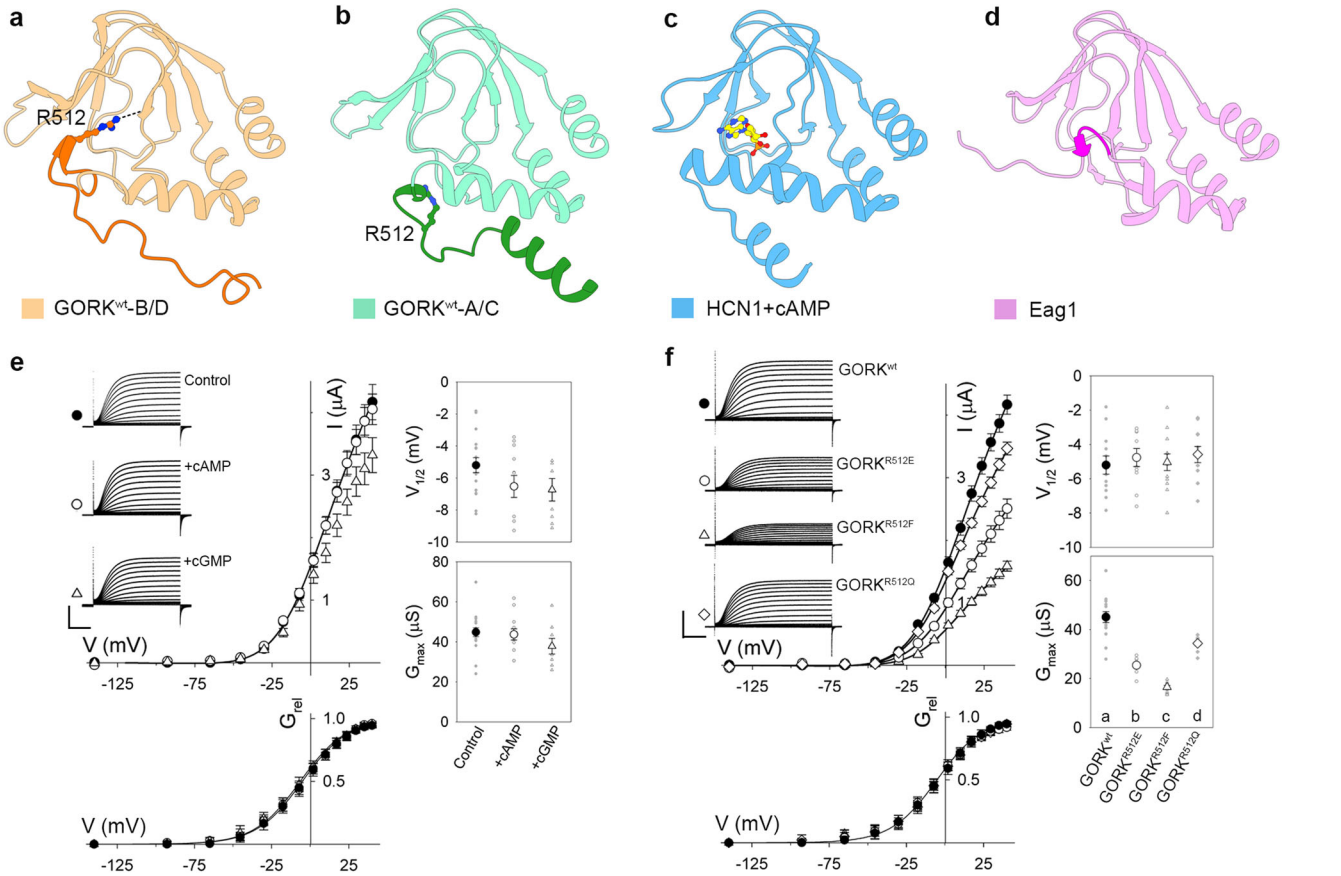

Fig. 3 | Intrinsic ligand in CNBHD. a, **b** The CNBHD domain from different subunits of GORK^{wt}. The A-linkers are indicated by darker colours. The residues R512 are shown as sticks. **c** The CNBD domain of HCN1 (PDB 5U6P). The bounded cAMP is shown as yellow sticks. **d** The CNBHD domain of Eag1 (PDB 5K7L). The 'intrinsic ligand' motif is indicated by darker colour. **e** Voltage clamp analysis of GORK^{wt} with 2 mM 8-bromo-cAMP and 8-bromo-cGMP added during recordings. Current–voltage curves (*centre, above*) and relative conductance–voltage curves (*centre, below*) are means ± SEM of $n > 9$ for each treatment. Gating parameters (*right*) of midpoint voltage ($V_{1/2}$) and maximum ensemble conductance (G_{max}) are from fittings to Eq. [1]. Relative conductance plots are overlaid with means ± SEM of tail currents after scaling to G_{max} taken from fittings to Eq. [1]. Representative voltage clamp traces (*insets, left*) are cross-referenced by symbol. Scale: vertical, 2 µA; horizontal, 1 s. Analysis (*right*) for each independent experiment (*small grey symbols*) and means ± SEM (*large symbols*) shows no significant effect on $V_{1/2}$ or G_{max} at $P < 0.05$. **f** Voltage clamp analysis of GORK^{wt} and the intrinsic ligand mutants GORK^{R512E}, GORK^{R512F}, and GORK^{R512Q}. Current–voltage curves (*centre, above*) and relative conductance–voltage curves (*centre, below*) are means ± SEM of $n > 11$ for each construct. Gating parameters (*right*) of midpoint voltage ($V_{1/2}$) and maximum ensemble conductance (G_{max}) are from fittings to Eq. [1]. Relative conductance plots are overlaid with means ± SEM of tail currents after scaling to G_{max} taken from fittings to Eq. [1]. Representative voltage clamp traces (*insets, left*) are cross-referenced by symbol. Scale: vertical, 2 µA; horizontal, 1 s. Gating analysis (*right*) for each independent experiment (*small grey symbols*) and means ± SEM (*large symbols*) showed no significant effect on $V_{1/2}$. Differences in G_{max} at $P < 0.001$ of the mutants indicated by lettering. Immunoblots are included in Supplementary Fig. 10. Source data are provided as a Source Data file.

T307 and V311 (Fig. 5b–d, Supplementary Movies 2 and 3). The C-linkers of GORK$^{\Delta 23}$-sym showed wider spacings at the 'elbow', a pattern also evident between the CNBHDs of neighbouring subunits (Fig. 5c and Supplementary Fig. 9c, d). Given the much-reduced energy barrier of the GORK$^{\Delta 23}$ mutation, we conclude that the structure is likely to represent a pre-open state primed for transition to a four-fold symmetry within the cytosolic region and opening of the pore.

Discussion

Although we have yet to resolve GORK in a bona fide open state, our results nonetheless highlight two coupling sites for gating centred around the C-linker, CNBHD, and the cytosolic face of the VSD. These structures and the conformations they assume are most evident when comparing GORK^{wt} with the GORK^{E317AD321A} and the N-terminal deletion mutants. Electrophysiological analysis showed that these mutants engender reductions in the energy barrier for gating and introduce current kinetics that are consistent with intermediates between the open and closed channel. Most striking are the effects of mutations in CSI that comprises a ring of interactions that build across each of the four channel subunits around the C-linkers and their interactions with the VSDs and S6 pore helices. The position of this ring, immediately below the opening to the channel pore and the base of the VSD, points to a critical role for the interactions in transit to the open channel conformation. This conclusion finds strong support with the extraordinarily slow current relaxations observed on mutating key C-linker and VSD residues (Fig. 2e, f). Additional contributions arise with an apparent intercalation of R512 from the A-linker within a pseudo-binding pocket of the CNBHD that contributes to CSII (Fig. 3). The latter interactions associate with the raised CNBHD that positions it against the C-linker and VSD, and they engender a shift of the VSD within the plane of the membrane and away from the PD (Supplementary Movies 1 and 2). Such effects are understood if the interactions jointly constrain the conformational freedom of the CNBHD and VSD: loss of this constraint, in the GORK^{T125A} and GORK^{L474A} mutants, then allows additional conformations that give rise to the shoulder in activation kinetics (Fig. 2i).

The conformational difference of GORK^{E317AD321A} with the wild-type structure is reminiscent of the transition between apo- and cNMP-

https://doi.org/10.1038/s41467-025-57287-7

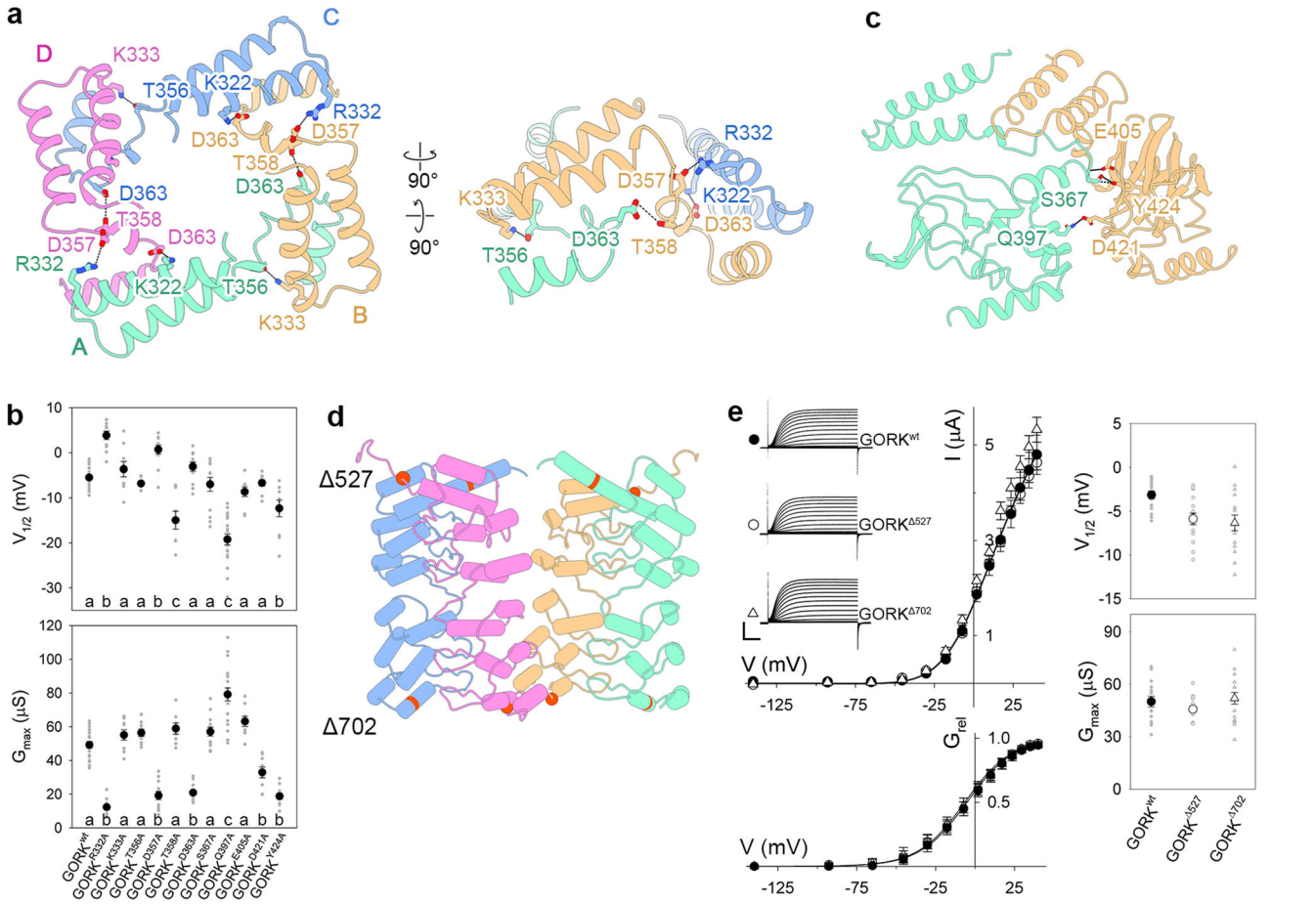

Fig. 4 | Tetrameric interface in cytosolic region. a Top and side views of the C-linker ring of the GORK tetramer, with each subunit individually coloured. Key residues are shown as sticks. **b**, Summary of voltage clamp analysis for GORK^{wt} and mutants of potential interacting residues within the C-linker and CNBHD domains. Data for $V_{1/2}$ and G_{max} are shown for each independent experiment (*small grey symbols*, $n > 9$ for each mutant) and their means ± SEM (*large symbols*). Significant differences indicated by lettering at $P < 0.002$. **c** Tetrameric interface formed by CNBHD domains of neighbouring subunits. **d** Tetrameric interface formed by ANK domains. The sites of Δ527 and Δ702 truncations are indicated by red spheres. **e** Voltage clamp analysis of GORK^{wt} and the C-terminal deletion mutants GORK^{Δ527} and GORK^{Δ702}. Current–voltage curves (*centre, above*) and relative conductance–voltage curves (*centre, below*) are means ± SEM of $n > 12$ for each treatment. Gating parameters (*right*) of midpoint voltage ($V_{1/2}$) and maximum ensemble conductance (G_{max}) are from fittings to Eq. [1]. Relative conductance plots are overlaid with means ± SEM of tail currents after scaling to G_{max} taken from fittings to Eq. [1]. Representative voltage clamp traces (*insets, left*) are cross-referenced by symbol. Scale: vertical, 2 μA; horizontal, 1 s. Data for $V_{1/2}$ and G_{max} for each construct (*small grey symbols*) are shown with means ± SEM (*large symbols*) cross-referenced by symbol. No significant differences were observed at $P < 0.05$. Fittings of the current- and conductance-voltage plots for GORK^{wt} shown (*centre, above and below*) for visual guidance. Immunoblots are included in Supplementary Fig. 10. Source data are provided as a Source Data file.

bound states of cyclic nucleotide-gated ion channels that bias these channels for enhanced sensitivities to voltage[17]. Furthermore, as we have observed, N-terminal deletions of GORK exhibit partial dilation of the pore. These structures associate with substantial shifts in the voltage-dependence for gating to favour the open channel, and they lend support to the idea of a pre-open conformation. In this state, the channel assumes a four-fold symmetry of kinked C-linkers with the CNBHDs raised and positioned against the corresponding C-linkers and VSDs. Thus, if dilation of the C-linker ring must occur in conjunction with movement of the VSD, it is tempting to view the states we have resolved as snapshots of intermediate stages revealing a set of mechanical 'latches' that must be engaged for the channel to open.

How the cytosolic N-terminus may interact within these structures remains to be resolved. Nonetheless, insertion of the N-terminus below the pore is likely to assume the role of a 'safety catch' to CSI and constrain its transitions to disfavour conformations leading to the open channel. Equally uncertain is the identity of the critical residues with which the N-terminus interacts. Nor do our data speak to the question of how these interactions might couple to the K^+ sensitivity of the channel gate. Previous studies had shown that sequences of alternating charges along the N-terminus engage in a 'fireman's grip' to form clusters of GORK channels and that clustering and gating are functionally linked through the N-terminus[14,15]. It may also prove useful to compare these findings with those of other CNBD channels for which gating is altered by N- and C-terminal regulatory domains (Supplementary Fig. 3). Among these an N-terminal domain of the KCNH channels, including the EAG, ERG and ELK channels, is thought to operate with intrinsic-ligand binding of the CNBD to promote channel activation and slow its deactivation[36,38,39]. We note that intercalation of the mammalian HCN1 N-terminus adjacent the C-linker appears to introduce contact points that couple cAMP binding to promote voltage-dependent gating of the channel[18,40]. So, we are tempted to speculate that analogous coupling interactions find roles in GORK for its gating with voltage and K^+.

It remains intriguing that each of the structures resolved to date has revealed a pore that is partially or fully closed. Yet each conformation nonetheless shows the VSD in the 'up' conformation that associates with the open channel. With some notable exceptions, the

https://doi.org/10.1038/s41467-025-57287-7

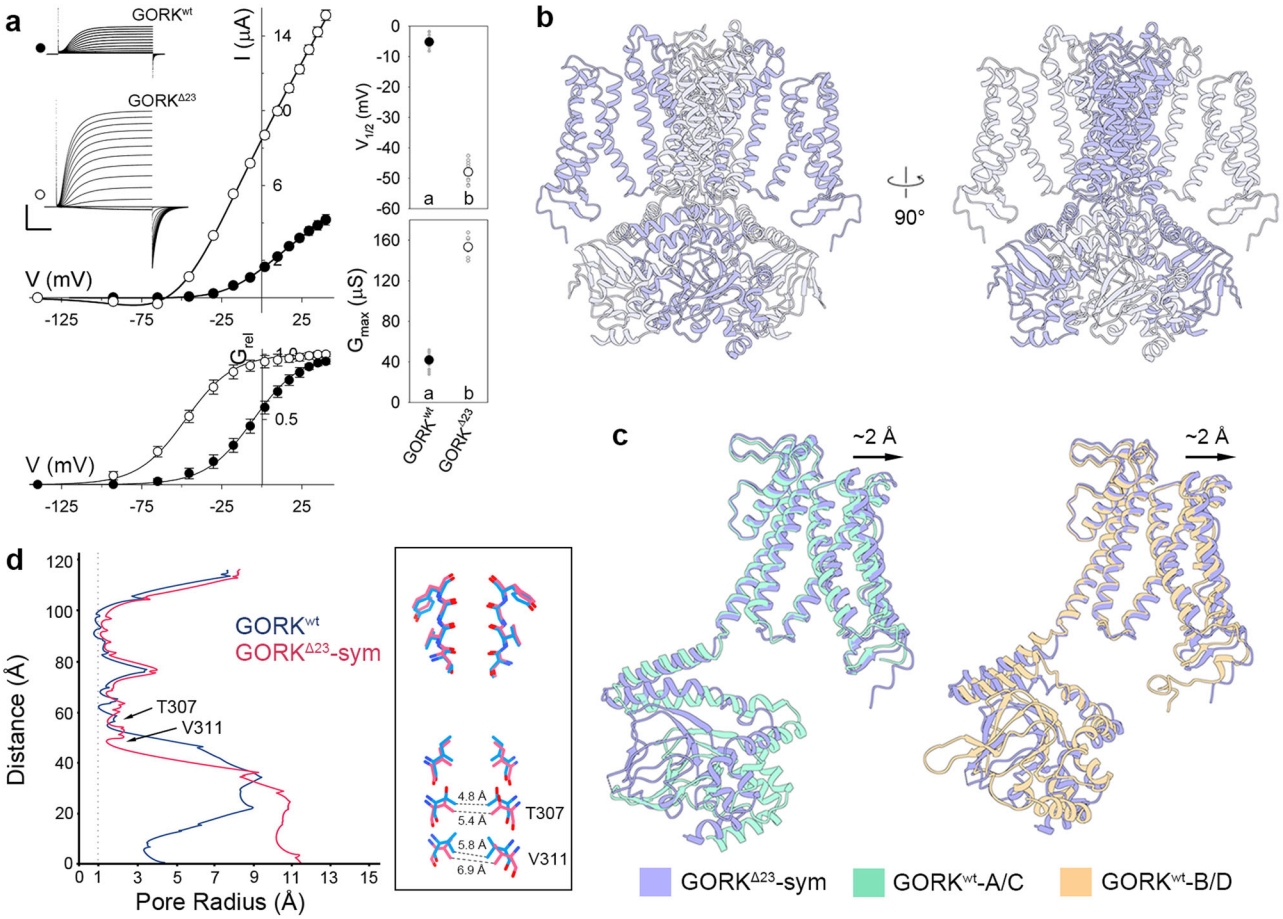

Fig. 5 | GORK$^{\Delta 23}$ adopts an apparent pre-open state. a Voltage clamp analysis of GORK^{wt} and N-terminal deletion mutant GORK$^{\Delta 23}$. Current–voltage (*centre, above*) and relative conductance–voltage curves (*centre, below*) curves are means ± SEM of $n > 15$ for each construct. Gating parameters (*right*) of midpoint voltage ($V_{1/2}$) and maximum ensemble conductance (G_{max}) are from fittings to Eq. [1]. Relative conductance plots are overlaid with means ± SEM of tail currents after scaling to G_{max} taken from fittings to Eq. [1]. Representative voltage clamp traces (*insets, left*) are cross-referenced by symbol and show accelerated activation and slowed deactivation. Scale: vertical, 4 μA; horizontal, 1 s. Gating analysis (*right*) for each independent experiment (*small grey symbols*) and means ± SEM (*large symbols*) shows a large negative shift in $V_{1/2}$ and a 4-fold increase in G_{max} for GORK$^{\Delta 23}$ relative to GORK^{wt}. Lettering indicates significant differences at $P < 0.001$. Fittings shown for comparison. Note the smaller inward current at −68 and −92 mV, negative of the K^+ equilibrium voltage. Immunoblots are included in Supplementary Fig. 10. Source data are provided as a Source Data file. **b** Overall structure of GORK$^{\Delta 23}$-sym, with diagonal subunits coloured in light and dark purple for clarity. **c** Structural difference between GORK^{wt} (green and yellow) and GORK$^{\Delta 23}$-sym (purple) subunits. The arrows indicate the VSD movement. **d** Pore radius of GORK^{wt} and GORK$^{\Delta 23}$-sym calculated using MOLE. The constricting residues are labelled.

VSDs of most K^+ channel structures resolved to date are tightly linked to the state of the pore, whether in the open or closed state[11,19,41]. By contrast, several CNBD/CNBHD channels appear to show a much weaker coupling between the VSD and channel pore. The mammalian HCN1 channel has been resolved with the pore both open and closed, in both cases with the VSD in the up position[18,42,43], leading to suggestions of a 'domino-like' sequence of transitions that connect voltage with channel activities so that VSD conformation is only indirectly connected to that of the pore[42,44].

While there is little doubt of a weak connection between VSD conformation and the open pore of GORK, our observations also challenge the perception of gating as a fixed, domino-like progression of conformational changes that must occur in sequence. Notably, the alternate conformations arising between the CNBHD and C-linker, and the associated, outward displacements of the VSD suggest instead that each may operate as semi-independent mechanical 'latches'. A detailed kinetic analysis of GORK remains outstanding. Nonetheless, the gating kinetics of GORK and its mutants are consistent with single-channel studies of the very close homologue SKOR, the second of the two outward-rectifying K^+ channels in Arabidopsis. Lifetime analysis of SKOR gating showed that the channel relaxes to a long-lived closed state - a 'locked closed' state - in millimolar K^+ that is evident even when the membrane is strongly depolarised[27]. In other words, it appears that the VSD transitions of GORK, like SKOR, are necessary but not sufficient to achieve the open state of the channel. Again, this behaviour fits a model of GORK gating that comprises a compound, mechanical latch with multiple steps that depend on separate inputs and operate semi-independently (Fig. 6).

Finally, our findings uncover two domains of the GORK channel that are certain to provide new targets for bioengineering. Previous studies demonstrated the potential of K^+ flux manipulations for improving water use efficiency and carbon assimilation by accelerating stomatal opening and closing[15,45]. Horaruang et al. [15] identified mutations within the GORK N-terminus that reduced the K^+ affinity for K^+ inhibition of gating, shifting the voltage dependence for channel activity to more negative voltages. The effect was to enhance the capacity for K^+ efflux at voltages positive of E_K and also to introduce a new conductance for K^+ influx at voltages negative of E_K. By enhancing K^+ flux behind stomatal movements, the GORK N-terminal mutants promoted both water use efficiency and assimilation under field-like conditions of fluctuating light: they accelerated stomatal opening with increases in light, thereby reducing stomatal limitation of CO_2 uptake

https://doi.org/10.1038/s41467-025-57287-7

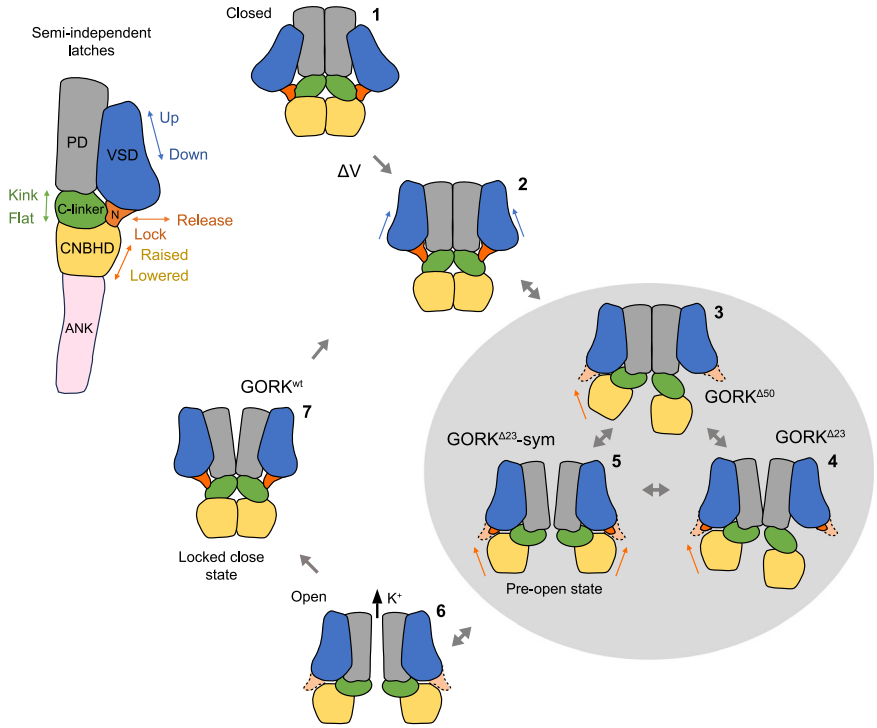

Fig. 6 | A semi-independent latch mechanism for GORK gating. GORK K^+ channel subunit structure (*top left*) comprising N-terminus (N), pore (PD) and voltage-sensor (VSD) domains, C-linker (C-linker), CNBHD (CNBHD) and ankyrin (ANK) domains, condensed for illustrative purposes. Only two of four subunits of the functional channel shown for clarity, omitting the ANK domain (*right and below*). For channel opening, each of four semi-independent conformational elements converge through state transitions (numbered conformations) to open the channel. Membrane depolarisation (①→②) drives the VSD outward to the up conformation. Relaxation of the N-terminus interchanges loosely with outward movement of the CNBHD to the raised conformation and an open, fourfold symmetry in the C-linker (③–⑤), not in a particular order. The raised CNBHD promotes lateral movement of the VSD away from the pore and facilitates channel opening (⑥). High K^+ outside favours transition to long-lived (locked closed) states (⑦). Retaining part of the N-terminus (dashed and solid N-terminus) may help stabilise the $GORK^{\Delta 23}$ and $GORK^{\Delta 23}$-sym conformations. The cryo-EM structures of $GORK^{\Delta 50}$, $GORK^{\Delta 23}$ and $GORK^{\Delta 23}$-sym may represent semi-independent conformations leading through a pre-open conformation to the open channel conformation and the initial $GORK^{wt}$ structure to the locked closed conformation. Conformations ①, ② and ⑥ are inferred from general knowledge of K^+ channel function, and the model conforms broadly with single-channel data for the GORK homologue SKOR[27] and the macroscopic kinetics described here.

to the leaf, and they accelerated the rate of closing, so reducing water loss with decreases in light by better matching stomatal movements to the reduced photosynthetic carbon assimilation when light was limiting[46]. Most important, Horaruang et al.[15] showed, by mechanistic modelling and experiment, that displacing $V_{1/2}$ by −20 mV and more relative to the wild-type channel was necessary and sufficient to achieve these gains in water use efficiency and carbon assimilation. Clearly similar, indeed greater, displacements in $V_{1/2}$ are realised with mutations of both CSI and CSII. Thus, it is plausible that further gains may be possible by targeting these sites. It remains now to assess the scope for such gains in the whole plant and whether combined manipulations of GORK gating might facilitate even greater gains in K^+ flux for stomatal movements.

Methods

Molecular cloning and mutagenesis

The gene encoding GORK (At5g37500, Uniprot Q94A76) was amplified from *Arabidopsis thaliana* complementary DNA as described previously[14]. For protein purification, the full-length GORK DNA sequence was subcloned into pFastBac vector containing a C-terminal GFP-His tag and TEV protease cleavage site. The mutations and N-terminal truncations were generated using two-step PCR with an initial amplification followed by DpnI digestion and a second round of re-amplification. For electrophysiology, we used Gateway Entry clones from previous work[14,47]. GORK truncations were created to include Gateway Entry sites and point mutations were generated by site-directed and overlapping PCR mutagenesis[48]. Entry clones in pDONR207 for Gateway reactions[49] were used throughout and all Entry clones verified by restriction digestion and sequencing. Destination clones were generated in pGT-myc-Dest with an extended C-terminal myc-tag of 21 residues and the expression clones were linearised for in vitro transcription and oocyte expression[31,50]. Primers used are listed in Supplementary Tables 1 and 2.

Expression and purification of proteins

GORK and its mutants were expressed in Sf9 insect cells after baculovirus transfection. After expression, the Sf9 cells were pelleted, frozen in liquid nitrogen and resuspended in buffer A (20 mM Tris pH 7.5, 150 mM KCl) supplemented with 1 mM phenylmethylsulfonyl fluoride (PMSF), 2 mM tris(2-carboxyethyl)phosphine (TCEP), 5 µg/mL aprotinin, 1.3 µg/mL pepstatin A, 0.5 µg/mL leupeptin, 1 mM benzamidine, 2 mM $MgCl_2$ and 5 µg/mL DNase I. Then 1% dodecyl maltoside (DDM) and 0.2% CHS was added before incubation at 4 °C for 3 h. Insoluble membranes were removed by ultracentrifugation at 150,000 *g* for 70 min; the supernatant was added to NHS-activated Sepharose beads (GE Healthcare) coupled to GFP nanobody[51] at 4 °C for 1 h. The beads were washed with 20 mM Tris-HCl pH 7.5, 150 mM KCl, 0.05% GDN, 2 mM TCEP and then incubated overnight with TEV protease at 4 °C to remove C-terminal GFP tag. The GORK protein was collected and concentrated for further purification by size-exclusion chromatography (SEC, Superose 6 increase 10/300 GL, GE Healthcare) equilibrated with buffer C (20 mM Tris-HCl pH 7.5, 150 mM KCl, 0.02% GDN, 2 mM TCEP). The peak fractions were collected and concentrated to 3-4 mg/mL for cryo-EM sample preparation.

For cells expressing GORK N-terminal truncations, the pellet was first suspended using hypotonic buffer of 20 mM Tris, pH 7.5, 10 mM KCl, 1 mM PMSF, benzamidine, and protease inhibitors for 45 min. The cell lysate was the spun at 39,800 *g* for 30 min to sediment crude membranes. The membrane pellet was homogenised and solubilized in 1% DDM + 0.2% CHS, 20 mM Tris pH 7.5, 10 or 10 mM KCl plus 40 mM NaCl, 1 mM PSMF, 2 mM TCEP, benzamidine, and protease inhibitors at 4 °C for 1 h. Insoluble membranes were removed by ultracentrifugation at 39,800 *g* for 30 min, with the subsequent steps as described above.

Cryo-EM sample preparation and data collection

To prepare samples for cryo-EM analysis, 3.5 µL protein was applied to glow-discharged carbon grids (Quantifoil Cu R1.2/1.3 400 mesh). Grids were blotted for 3 s with Grade 597 Filter Paper (Whatman) and plunge-frozen in liquid ethane cooled by liquid nitrogen using a Vitrobot Mark IV (Thermo Scientific) at 8 °C and 100% humidity.

Datasets for GORK^{wt} and GORK^{E317AD321A} were collected on a Titan Krios (Thermo Scientific) transmission electron microscope operated at 300 kV and equipped with a K3 direct electron detector (Gatan) and Gatan imaging filter (GIF). For GORK^{wt}, 6866 movie stacks were automatically acquired in super-resolution mode (81,000× magnification) using SerialEM software, with a set defocus range from −1.2 mm to −2.2 mm. Each stack was exposed for 2 s, resulting in 40 frames and a total dose of 58.3 $e^-/Å^2$. For GORK^{E317AD321A}, 3334 movie stacks were automatically acquired in super-resolution mode (130,000× magnification) using EPU software, with a set defocus range from −1.0 mm to −2.0 mm. Each stack was exposed for 2 s, resulting in 40 frames and total irradiation of 57.8 $e^-/Å^2$. Datasets for GORK^{Δ50} and GORK^{Δ23} were collected on a Titan Krios G4 transmission electron microscope with a Falcon 4 direct electron detector and Selectrix X imaging filter (Thermo Scientific) operated at 300 kV in zero-loss mode with a slit width of 20 eV. Sets of 4683 and 4045 movie stacks, respectively, were automatically acquired in super-resolution mode (130,000× magnification) using EPU software with a defocus range from −1.0 mm to −2.0 mm. Each stack was exposed for 3.51 s, resulting in 1080 frames and total dose of 49.3 $e^-/Å^2$.

Data processing

The data processing workflow and statistics are summarised in Supplementary Figs. 1 and 6–8 and Supplementary Table 3. Raw movies were first motion-corrected using MotionCor2[52] and, for Falcon 4 data, frames were aligned using motion correction in RELION 3.1[53]. The resulting dose-weighted micrographs were imported to cryoSPARC v3[54] for patch-based contrast transfer function (CTF) estimation. After blob picker or template picker selection, particles were extracted for each dataset. Junk particles were removed by multiple rounds of 2D classification. The initial 3D model was generated using ab initio reconstruction. Subsequent multi-class heterogenous refinement and resolution gradient classification was performed to clean the particles, and the best classes were used for non-uniform refinement without imposing symmetry. Local refinement or CTF refinement was performed to further process particles until a high-quality map was generated. The overall resolution of each map was determined by the gold-standard Fourier Shell Correlation (FSC) 0.143 criterion. Local resolution estimation of each map was generated by cryoSPARC.

For the dataset of GORK^{wt}, the heterogenous refinement generated one major class. After gradient resolution refinement, the best class generate a high-quality map with an overall resolution of 3.00 Å. Local refinement was performed with a soft mask around cytosolic region to further improve the map quality of ankyrin-repeat domain.

For the dataset of GORK^{E317AD321A}, the non-uniform refinement yielded a map with strong densities of transmembrane region. Further 3D classification used a mask focusing on PD and C-linker and generated three classes. The class showing different conformation of C-linker domain was further processed with non-uniform refinement and generated a map with an overall resolution of 3.14 Å.

For the dataset of GORK^{Δ50}, the non-uniform refinement yielded a map with strong densities of transmembrane region and CNBHD domain. Further 3D classification generated three classes, with two classes showing three lifted CNBHD and one class showing two lifted CNBHD. The particles showing three lifted CNBHD were combined and further processed with non-uniform refinement and generated a map with an overall resolution of 2.60 Å.

For the dataset of GORK^{Δ23}, heterogenous refinement generated two good classes, with one class showing C2 symmetry in cytosolic region while the other showing C4 symmetry. The particles from these good classes were combined and further processed with 3D variable analysis, yielding eight clusters. The C4-symmetry classes from heterogenous refinement and 3D variable analysis were combined, and duplicate particles were removed. Further process using non-uniform refinement and C4 symmetry generated a map with strong density of transmembrane region and CNBHD domain. Symmetry expansion and local refinement were performed to further improved the map quality and generated a map with an overall resolution of 2.43 Å.

Model building and structure refinement

The atomic model of GORK was built based on an initial model predicted by AlphaFold II[55], and manual model building and adjustments were carried out with COOT[56]. The resulting model was refined using a real space refinement module from PHENIX[57] with secondary structure and geometry restraints applied. The structures were validated with MolProbity[58], and refinement statistics can be found in Supplementary Table 3. All structure figures were prepared in ChimeraX[59].

Electrophysiology

K^+ channels expressed in *Xenopus* oocytes were recorded by two-electrode voltage clamp[14,31,47] using Henry's EP suite (v. 3.6.5.5, Y-Science, Glasgow, UK). Capped mRNAs (cRNAs) were generated from linearised oocyte-expression plasmids (HiScribe® T7 ARCA mRNA Kit, E2065S, New England Biolabs) and were injected at 25 ng/oocyte. Recordings were carried out 72 h after injection and oocytes were collected and analysed for protein expression. For recordings, oocytes were superfused with 10 mM K^+ in modified ND96 buffer with 1.8 mM $MgCl_2$, 1.8 mM $CaCl_2$ and 10 mM HEPES-NaOH, pH 7.2 adjusted for osmotic balance[47,60]. Measurements with the membrane-permeant 8-bromo-cAMP and 8-bromo-cGMP were carried out on the same oocytes before and 25–30 min after additions. Voltage was clamped in cycles with 4-s to 6-s, positive-going steps between -120 mV and +40 mV. Steps were from a holding voltage of −140 mV or −160 mV, well negative of the K^+ equilibrium voltage E_K, followed by an extended step back to the holding voltage.

Background currents were subtracted and K^+ currents were analysed using Henry's EP suite and SigmaPlot 11.2 (Systat Software, Inc., USA) as described previously[14,61–63]. Steady-state current, *I*, was fitted by joint, non-linear least-squares using a Marquardt-Levenberg algorithm to a Boltzmann function of the form

$$I = \frac{G_{max}(V - E_K)}{1 + e^{\delta F(V_{1/2} - V)/RT}} \quad (1)$$

where G_{max} is the maximum ensemble channel conductance, V is the membrane voltage, $V_{1/2}$ is the midpoint voltage for gating, δ is the apparent gating charge or voltage sensitivity, and F, R, and T have their usual meanings. Relative conductances, G_{rel} (=G/G_{max}), were derived from Eq. [1] as

$$G_{rel} = \frac{1}{1 + e^{\delta F(V_{1/2} - V)/RT}} \quad (2)$$

and were also plotted directly from tail currents recorded on returning to the holding voltage, either −140 or −160 mV, after scaling the maximum tail currents to G_{max} from fittings to Eq. [1]. The close match between G_{rel} derived from fittings to Eqs. [1] and [2] when compared to the relative tail current amplitudes confirmed the validity of assuming a constant conductance to the open-channel current, independent of voltage, despite the asymmetry in K^+ concentrations across the membrane. This conclusion was also supported by instantaneous current-voltage analysis of $GORK^{wt}$ and the most negative-shifted of the mutants, $GORK^{\Delta 23}$ (Supplemental Fig. 11), much as shown previously for GORK[8] and its homologue in Vicia guard cells[12].

Current relaxation kinetics were fitted similarly by joint, non-linear least-squares minimisation to a simple exponential function to extract the deactivation kinetics. For activation, currents were analysed using the in-built functions of Henry's EP suite to calculate half-times at each clamp voltage from normalised current relaxations.

Immunoblot analysis

Proteins expressed in oocytes were analysed from oocytes collected after electrophysiological recordings[47]. Immunoblots were analysed following standard protocols[48] using rabbit αGORK antibody[14] or αmyc antibody (ab9106, Abcam, Cambridge UK) at 1:4000 or 1:10,000 dilutions and goat anti-rabbit horseradish peroxidase-conjugated secondary antibodies (ab6721, Abcam) at 1:10,000 dilution. Antibody-bound protein bands were visualised by chemiluminescence using HRP substrate (peroxide) luminol (Thermo Scientific, Cat. 34075). Ponceau staining was used as a control to verify an equal loading. Chemiluminescent signals were acquired (Fusion spectra, Vilber Lourmat) at 600 dpi resolution and quantified using ImageJ v1.54f (rsbweb.nih.gov/ij/).

Statistics

All results are reported as means ± SEM of *n* independent experiments. Significance was determined by *t*-test and Analysis of Variance (ANOVA), as appropriate, with post-hoc analysis (Tukey). Significant differences are indicated by different lettering at $P < 0.05$ unless otherwise stated.

Reporting summary

Further information on research design is available in the Nature Portfolio Reporting Summary linked to this article.

Data availability

The cryo-EM density maps of $GORK^{wt}$, $GORK^{E317AD332IA}$, $GORK^{\Delta 50}$, and $GORK^{\Delta 23}$ have been deposited in the Electron Microscopy Data Bank (EMDB) under accession codes EMD-61061, EMD-61062, EMD-61063, and EMD-61064, respectively. The corresponding atomic coordinates have been deposited in the Protein Data Bank (PDB) under accession codes PDB 9J0X, 9J0Y, 9J0Z, and 9J10, respectively. Source data are provided with this paper.

References

1. Assmann, S. M. & Jegla, T. Guard cell sensory systems: recent insights on stomatal responses to light, abscisic acid, and CO2. *Curr. Opin. Plant Biol.* **33**, 157–167 (2016).
2. Jezek, M. & Blatt, M. R. The Membrane Transport System of the Guard Cell and Its Integration for Stomatal Dynamics. *Plant Physiol.* **174**, 487–519 (2017).
3. Lawson, T. & Matthews, J. In *Annual Review of Plant Biology* Vol. 71 *Annual Review of Plant Biology* (ed Merchant, S. S.) 273–302 (2020).
4. Very, A. A. & Sentenac, H. Molecular mechanisms and regulation of K^+ transport in higher plants. *Annu. Rev. Plant Biol.* **54**, 575–603 (2003).
5. Wang, Y. & Wu, W. H. In Annual Review of Plant Biology, *Vol 64* Vol. 64 *Annual Review of Plant Biology* (ed Merchant, S. S.) 451–476 (2013).
6. Lebaudy, A. et al. Plant adaptation to fluctuating environment and biomass production are strongly dependent on guard cell potassium channels. *Proc. Natl Acad. Sci. USA* **105**, 5271–5276 (2008).
7. Hosy, E. et al. The Arabidopsis outward K^+ channel GORK is involved in regulation of stomatal movements and plant transpiration. *Proc. Natl Acad. Sci. USA* **100**, 5549–5554 (2003).
8. Ache, P. et al. GORK, a delayed outward rectifier expressed in guard cells of Arabidopsis thaliana, is a K^+ -selective, K^+ -sensing ion channel. *FEBS Lett.* **486**, 93–98 (2000).
9. Blatt, M. R. A charged existence: A century of transmembrane ion transport in plants. *Plant Physiol.* https://doi.org/10.1093/plphys/kiad630 (2024).
10. Alvim, F. S. L., Alvim, J., Harvey, A. L. & Blatt, M. R. Speedy stomata of a C_4 plant correlate with enhanced K^+ channel gating. *Plant Cell Environ.* **47**, 817–831 (2024).
11. Lefoulon, C. The bare necessities of plant K+ channel regulation. *Plant Physiol.* **187**, 2092–2109 (2021).
12. Blatt, M. R. & Gradmann, D. K^+ -sensitive gating of the K^+ outward rectifier in Vicia guard cells. *J. Membr. Biol.* **158**, 241–256 (1997).
13. Blatt, M. R. Potassium-dependent bipolar gating of potassium channels in guard cells. *J. Membr. Biol.* **102**, 235–246 (1988).
14. Eisenach, C., Papanatsiou, M., Hillert, E. K. & Blatt, M. R. Clustering of the K^+ channel GORK of Arabidopsis parallels its gating by extracellular K+. *Plant J.* **78**, 203–214 (2014).
15. Horaruang, W. et al. Engineering a K^+ channel 'sensory antenna' enhances stomatal kinetics, water use efficiency and photosynthesis. *Nat. Plants* **8**, 1262–1274 (2022).
16. Nguyen, T. B.-A., Lefoulon, C., Nguyen, T.-H., Blatt, M. R. & Carroll, W. Engineering stomata for enhanced carbon capture and water-use efficiency. *Trends Plant Sci.* **28**, 1290–1309 (2023).
17. Lee, C.-H. & MacKinnon, R. Structures of the human HCN1 hyperpolarization-activated channel. *Cell* **168**, 111–120, (2017).
18. Porro, A. et al. The HCN domain couples voltage gating and cAMP response in hyperpolarization-activated cyclic nucleotide-gated channels. *Elife* **8**, e49672 (2019).
19. Clark, M. D., Contreras, G. F., Shen, R. & Perozo, E. Electromechanical coupling in the hyperpolarization-activated K+ channel KAT1. *Nature* **583**, 145 (2020). -+.
20. James, Z. M. et al. CryoEM structure of a prokaryotic cyclic nucleotide-gated ion channel. *Proc. Natl Acad. Sci. USA* **114**, 4430–4435 (2017).
21. Whicher, J. R. & MacKinnon, R. Structure of the voltage-gated K^+ channel Eag1 reveals an alternative voltage sensing mechanism. *Science* **353**, 664–669 (2016).
22. Xue, J., Han, Y., Zeng, W. Z., Wang, Y. & Jiang, Y. X. Structural mechanisms of gating and selectivity of human rod CNGA1 channel. *Neuron* **109**, 1302 (2021).
23. Li, S. et al. Cryo-EM structure reveals a symmetry reduction of the plant outward-rectifier potassium channel SKOR. *Cell Discov.* **9**, 67–67 (2023).
24. Lu, Y. M. et al. Structural basis for the activity regulation of a potassium channel AKT1 from Arabidopsis. *Nat. Commun.* **13**, 5682 (2022).
25. Zhou, Y. F., Morais-Cabral, J. H., Kaufman, A. & MacKinnon, R. Chemistry of ion coordination and hydration revealed by a K^+ channel-Fab complex at 2.0 angstrom resolution. *Nature* **414**, 43–48 (2001).
26. Morais-Cabral, J. H., Zhou, Y. F. & MacKinnon, R. Energetic optimization of ion conduction rate by the K+ selectivity filter. *Nature* **414**, 37–42 (2001).

27. Johansson, I. et al. External K + modulates the activity of the Arabidopsis potassium channel SKOR via an unusual mechanism. *Plant J.* **46**, 269–281 (2006).
28. Dickinson, M. S., Pourmal, S., Gupta, M., Bi, M. & Stroud, R. M. Symmetry reduction in a hyperpolarization-activated homotetrameric ion channel. *Biochemistry* **61**, 2177–2181 (2022).
29. Xu, J. et al. A protein kinase, interacting with two calcineurin B-like proteins, regulates K + transporter AKT1 in Arabidopsis. *Cell* **125**, 1347–1360 (2006).
30. Li, L. G. & Luan, S. A Ca 2+ signaling pathway regulates a K + channel for low-K response in Arabidopsis. *Proc. Natl Acad. Sci. USA* **103**, 12625–12630 (2006).
31. Lefoulon, C., Waghmare, S., Karnik, R. & Blatt, M. R. Gating control and K+ uptake by the KAT1 K+ channel leaveraged through membrane anchoring of the trafficking protein SYP121. *Plant Cell Environ.* **41**, 2668–2677 (2018).
32. Jegla, T., Busey, G. & Assmann, S. M. Evolution and structural characteristics of plant voltage-gated K+ channels. *Plant Cell* **30**, 2898–2909 (2018).
33. Brelidze, T. I., Carlson, A. E., Sankaran, B. & Zagotta, W. N. Structure of the carboxy-terminal region of a KCNH channel. *Nature* **481**, 530–U147 (2012).
34. Haitin, Y., Carlson, A. E. & Zagotta, W. N. The structural mechanism of KCNH-channel regulation by the eag domain. *Nature* **501**, 444 (2013).
35. Brelidze, T. I., Gianulis, E. C., DiMaio, F., Trudeau, M. C. & Zagotta, W. N. Structure of the C-terminal region of an ERG channel and functional implications. *Proc. Natl Acad. Sci. USA* **110**, 11648–11653 (2013).
36. Zhao, Y. X., Goldschen-Ohm, M. P., Morais-Cabral, J. H., Chanda, B. & Robertson, G. A. The intrinsically liganded cyclic nucleotide-binding homology domain promotes KCNH channel activation. *J. Gen. Physiol.* **149**, 249–260 (2017).
37. Dreyer, I. et al. Assembly of plant Shaker-like K-out channels requires two distinct sites of the channel alpha-subunit. *Biophys. J.* **87**, 858–872 (2004).
38. Gustina, A. S. & Trudeau, M. C. hERG potassium channel gating is mediated by N- and C-terminal region interactions. *J. Gen. Physiol.* **137**, 315–325 (2011).
39. Muskett, F. W. et al. Mechanistic insight into human *ether-a-go-go* related Gene (hERG) K^+ channel deactivation gating from the solution structure of the EAG Domain. *J. Biol. Chem.* **286**, 6184–6191 (2011).
40. Saponaro, A. et al. Gating movements and ion permeation in HCN4 pacemaker channels. *Mol. Cell* **81**, 2929 (2021).
41. Palovcak, E., Delemotte, L., Klein, M. L. & Carnevale, V. Evolutionary imprint of activation: the design principles of VSDs. *J. Gen. Physiol.* **143**, 145–156 (2014).
42. Lee, C. H. & MacKinnon, R. Voltage sensor movements during hyperpolarization in the HCN channel. *Cell* **179**, 1582 (2019).
43. Burtscher, V. et al. Structural basis for hyperpolarization-dependent opening of human HCN1 channel. *Nat. Commun.* https://doi.org/10.1038/s41467-024-49599-x (2024).
44. Elbahnsi, A. et al. Interplay between VSD, pore, and membrane lipids in electromechanical coupling in HCN channels. *eLife* https://doi.org/10.7554/eLife.80303 (2023).
45. Papanatsiou, M. et al. Optogenetic manipulation of stomatal kinetics improves carbon assimilation and water use efficiency. *Science* **363**, 1456–1459 (2019).
46. Lawson, T. & Blatt, M. R. Stomatal size, speed, and responsiveness impact on photosynthesis and water use efficiency. *Plant Physiol.* **164**, 1556–1570 (2014).
47. Lefoulon, C. et al. Voltage-sensor transitions of the inward-rectifying K^+ channel KAT1 indicate a closed-to-open latching mechanism that is biased by hydration around the S4 alpha-helix. *Plant Physiol.* **166**, 960–975 (2014).
48. Karnik, R. et al. Arabidopsis Sec1/Munc18 protein SEC11 is a competitive and dynamic modulator of SNARE binding and SYP121-dependent vesicle traffic. *Plant Cell* **25**, 1368–1382 (2013).
49. Grefen, C. & Blatt, M. R. A 2in1 cloning system enables ratiometric bimolecular fluorescence complementation (rBiFC). *Biotechniques* **53**, 311–314 (2012).
50. Grefen, C. et al. A vesicle-trafficking protein commandeers Kv channel voltage sensors for voltage-dependent secretion. *Nat. Plants* **1**, 15108–15119 (2015).
51. Kirchhofer, A. et al. Modulation of protein properties in living cells using nanobodies. *Nat. Struct. Mol. Biol.* **17**, 133–U162 (2010).
52. Zheng, S. Q. et al. MotionCor2: anisotropic correction of beam-induced motion for improved cryo-electron microscopy. *Nat. Methods* **14**, 331–332 (2017).
53. Scheres, S. H. RELION: implementation of a Bayesian approach to cryo-EM structure determination. *J. Struct. Biol.* **180**, 519–530 (2012).
54. Punjani, A., Rubinstein, J. L., Fleet, D. J. & Brubaker, M. A. cryoSPARC: algorithms for rapid unsupervised cryo-EM structure determination. *Nat. Methods* **14**, 290 (2017).
55. Tunyasuvunakool, K. et al. Highly accurate protein structure prediction for the human proteome. *Nature* **596**, 590 (2021).
56. Emsley, P. & Cowtan, K. Coot:: model-building tools for molecular graphics. *Acta Crystallogr. Sect. D* **60**, 2126–2132 (2004).
57. Adams, P. D. et al. PHENIX: a comprehensive Python-based system for macromolecular structure solution. *Acta Crystallogr. Sect. D* **66**, 213–221 (2010).
58. Davis, I. W. et al. MolProbity: all-atom contacts and structure validation for proteins and nucleic acids. *Nucleic Acids Res.* **35**, W375–W383 (2007).
59. Pettersen, E. F. et al. UCSF ChimeraX: structure visualization for researchers, educators, and developers. *Protein Sci.* **30**, 70–82 (2021).
60. Grefen, C. et al. A novel motif essential for SNARE interaction with the K^+ channel KC1 and channel gating in Arabidopsis. *Plant Cell* **22**, 3076–3092 (2010).
61. Jezek, M. et al. Guard cell endomembrane Ca^{2+}-ATPases underpin a 'carbon memory' of photosynthetic assimilation that impacts on water use efficiency. *Nat. Plants* **7**, 1301–1307 (2021).
62. Chen, Z. H., Hills, A., Lim, C. K. & Blatt, M. R. Dynamic regulation of guard cell anion channels by cytosolic free Ca^{2+} concentration and protein phosphorylation. *Plant J.* **61**, 816–825 (2010).
63. Blatt, M. R. Electrical characteristics of stomatal guard cells: the contribution of ATP-dependent, "electrogenic" transport revealed by current-voltage and difference-current-voltage analysis. *J. Membr. Biol.* **98**, 257–274 (1987).

Acknowledgements

We thank Dr. Minhua Zhang (CAS Centre for Excellence in Molecular Plant Sciences core facility) for diagnostic cryo-EM analysis, Hui Zhao and Xiang Zhang (Fudan University), and Mingming Zhang (CAS Interdisciplinary Research Centre on Biology and Chemistry) for technical assistance in cryo-EM data collection. We also thank Naomi Donald, Amparo Ruiz-Prado, Cecile Lefoulon and George Boswell (Glasgow) for support in Xenopus handling, oocyte preparation and expression, and immunoblot analysis. This work was supported by grants from the Chinese Academy of Sciences (CAS) (XDB0630100 and 317GJHZ2022023GC to P.Z.), from the National Natural Science Foundation of China (32471249 to X.Z., and 32025020 to P.Z.), from Shanghai Science and Technology Commission (23310710100), from the UK Biotechnology and Biological Sciences Research Council (BB/T006153/1 and BB/T013508/1 to M.R.B. and BB/W001217/1, BB/X013383/1 and BB/Y010272/1 to M.R.B. and R.K.), and from the Royal Society, London, to R.K. (UF150364 and URF\R\211002).

Author contributions

P.Z. and M.R.B. conceived the project. P.Z., M.R.B., X.Z., W.C., T.B.A.N., and T.H.N. designed experiments. X.Z. carried out protein expression, sample preparation, and cryo-EM data collection with M.M., G.H., and X.H., and structural determinations guided by P.Z. with suggestions from M.R.B. W.C., T.B.A.N., and T.H.N. carried out electrophysiological experiments and analysed the results with M.R.B., R.K., and A.H. A.H. wrote software for electrophysiological data collection and analysis. Z.Y. contributed to grid sample preparation and screening. P.Z., M.R.B., X.Z., and T.B.A.N. wrote the paper. All authors edited and approved the paper.

Competing interests

The authors declare no competing interests.

Additional information

Supplementary information The online version contains supplementary material available at https://doi.org/10.1038/s41467-025-57287-7.

Correspondence and requests for materials should be addressed to Michael R. Blatt or Peng Zhang.

Peer review information *Nature Communications* thanks the anonymous reviewers for their contribution to the peer review of this work. A peer review file is available.

Reprints and permissions information is available at http://www.nature.com/reprints

Publisher's note Springer Nature remains neutral with regard to jurisdictional claims in published maps and institutional affiliations.

Open Access This article is licensed under a Creative Commons Attribution-NonCommercial-NoDerivatives 4.0 International License, which permits any non-commercial use, sharing, distribution and reproduction in any medium or format, as long as you give appropriate credit to the original author(s) and the source, provide a link to the Creative Commons licence, and indicate if you modified the licensed material. You do not have permission under this licence to share adapted material derived from this article or parts of it. The images or other third party material in this article are included in the article's Creative Commons licence, unless indicated otherwise in a credit line to the material. If material is not included in the article's Creative Commons licence and your intended use is not permitted by statutory regulation or exceeds the permitted use, you will need to obtain permission directly from the copyright holder. To view a copy of this licence, visit http://creativecommons.org/licenses/by-nc-nd/4.0/.

© The Author(s) 2025